THE JOURNAL OF PHYSICAL CHEMISTRY A

Article

Cite This: J. Phys. Chem. A 2019, 123, 1343−1352

pubs.acs.org/JPCA

Evaluating the Impact of Fluorination on the Electro-optical Properties of Cross-Conjugated Benzobisoxazoles

Published as part of The Journal of Physical Chemistry virtual special issue "William M. Jackson Festschrift".

Ramiro Chavez III,[†] Lily Diodati,[‡] David L. Wheeler,[†] Jessica Shaw,[†] Aimée L. Tomlinson,*[,‡] and Malika Jeffries-EL*[,†]

[†]Department of Chemistry, Boston University, 590 Commonwealth Avenue, Boston, Massachusetts 02215, United States

[‡]Department of Chemistry and Biochemistry, University of North Georgia, 82 College Circle, Dahlonega, Georgia 30041, United States

Supporting Information

ABSTRACT: Six 2,4,6,8-tetrarylbenzo[1,2-*d*:4,5-*d*′]bisoxazoles (BBOs) were synthesized: three bearing phenyl substituents at the 2- and 6-positions and three bearing perfluorophenyl groups at those positions. The influence of perfluoro-aryl group substitution on the physical, optical, and electronic properties of 2,4,6,8-tetrarylbenzo[1,2-*d*:4,5-*d*′]bisoxazoles (BBO) was evaluated using both experimental and theoretical methods. The density functional theory (DFT) model was found to be well-matched to the experimental optical data, as evidenced by the UV−vis spectra. Both cyclic voltammetry (CV) and ultraviolet photoelectron spectroscopy (UPS) were used to determine the position of the HOMO with varying results. The values obtained by CV were deeper than those obtained via UPS and correlated well with the theoretical calculations. However, the UPS values were more consistent with the expected outcomes for a system with segregated frontier molecular orbitals (FMOs). The UPS results are also supported by the electrostatic potential maps, which indicate that the electron density within the LUMO and HOMO is nearly completely localized along the 2,6- or 4,8-axis, respectively. The summation of the results indicates that strongly electron-withdrawing groups can be used to selectively tune the LUMO level with minor perturbation of the HOMO, something that is challenging to accomplish in typical donor−acceptor systems.

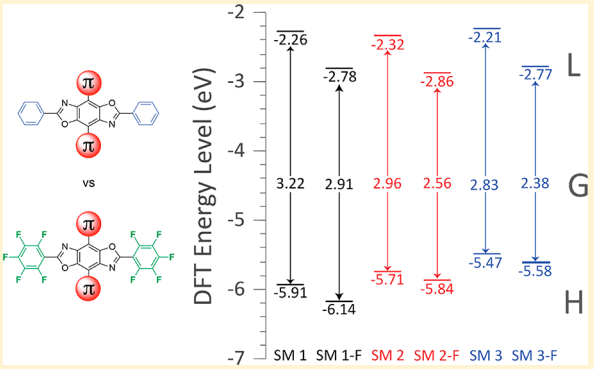

INTRODUCTION

Cross-conjugated organic molecules are a unique class of organic semiconductors that have spatially segregated frontier molecular orbitals (FMOs), allowing for semiselective tuning of the highest occupied molecular orbital (HOMO), or the lowest unoccupied molecular orbital (LUMO) via structural modification.[1] As a result, these "cruciforms" are useful materials for fundamental research on structure−property relationships in organic semiconductors. At the same time they are promising materials for a range of applications including molecular electronics,[2] organic field effect transistors (OFETs),[3] organic light emitting diodes (OLEDs), sensors,[4−7] and organic solar cells (OSCs).[8] All of these applications can benefit from the well-defined, defect free nature of a molecular species. Additionally, the opportunities for band gap and energy level engineering afforded by these systems is also very alluring as they can be optimized for use in specific applications.

It has been well-established that an effective method to tune the FMOs and band gaps of an organic semiconductor is by combining electron-donating and electron-withdrawing substituents within the same molecule.[9−11] One way to increase the electron-withdrawing nature of a substituent is through fluorination. Due to fluorine's electronegativity, the atom pulls electron density away from the aromatic π-system, stabilizing the FMOs. Such a lowering of the HOMO can increase the oxidative stability of the materials, while lowering the LUMO can transform a p-type organic semiconductor into a n-type or ambipolar one.[12] The small atomic radius of fluorine is minimally disruptive on the structure, but the polar nature of the carbon−fluorine bond increases the dipole moment, modifies the intramolecular interactions, and potentially enhances charge transport.[13,14] Furthermore, the quadrupole moments of perfluorinated acenes are opposite in sign of the analogous acenes, thus significantly tuning the orbital energetics and intermolecular overlaps.[15−17] Most interestingly, fluorination has been shown to greatly impact the optical transitions of conjugated organic molecules; however, the

Received: August 9, 2018
Revised: December 5, 2018
Published: January 25, 2019

DOI: 10.1021/acs.jpca.8b07778
J. Phys. Chem. A 2019, 123, 1343−1352

nature of this modification varies depending on the nature of the molecule.[14,18] For example, in comparison to the corresponding nonfluorinated derivatives, bathochromic shifts in the absorption spectra were observed for fluorinated oligothiophenes,[19] while hypsochromic shifts were seen for oligoacenes.[12,18]

In this work, we evaluated the impact of fluorine substitution on a series of benzo[1,2-*d*:4,5-*d*′]bisoxazole (BBO)-based cruciforms (Charts 1 and 2). As a result of the two,

Chart 1. Numbering for Benzobisoxazole Ring System and Axes

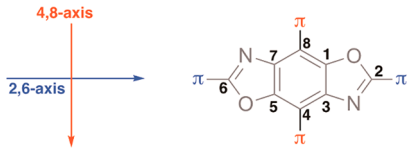

Chart 2. Structures of BBO Cruciforms

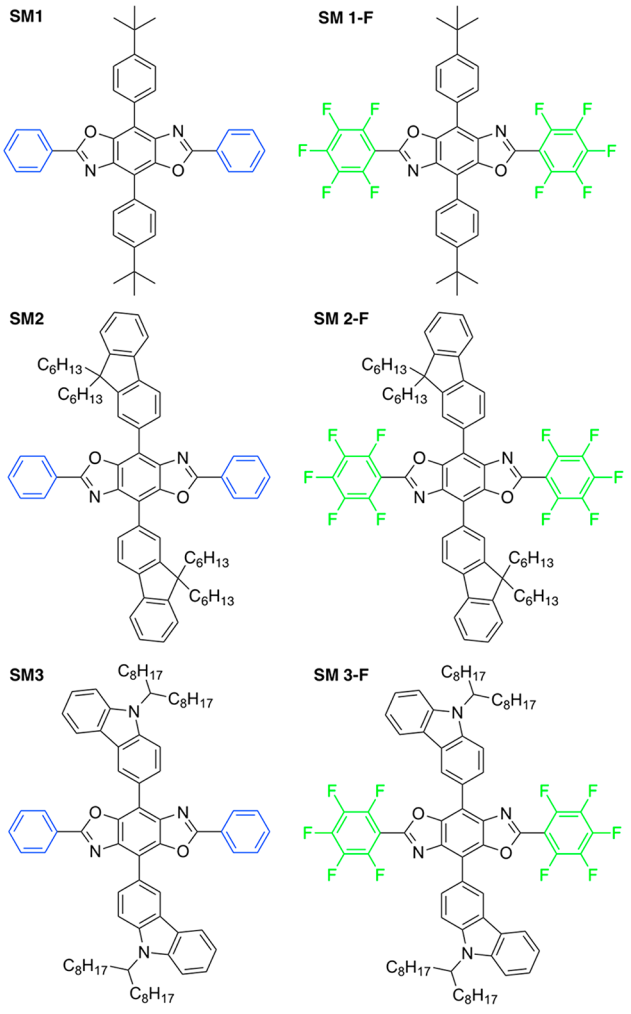

nonequivalent conjugation axes within this system, the nature and placement of substituents can greatly impact either the HOMO level or the LUMO level semi-independently.[5,20−24] Specifically, the electron density of the HOMO is localized along the 4,8-axis when electron-rich substituents are placed there, whereas the electron density of the LUMO is localized along the 2,6-axis when less electron-rich substituents are placed there.[22] However, in previous studies, the impacts of strongly electron-withdrawing groups were not investigated. It is our hypothesis that the incorporation of such a group would enhance the spatial segregation of the FMOs. Within these systems, we see near complete segregation in some instances, thus demonstrating the potential of this approach for the design of tunable conjugated materials.

EXPERIMENTAL AND THEORETICAL METHODS

Computational Details. Calculations on the molecules studied in this work were performed using the Gaussian 09[25] with the GaussView 6 GUI interface program package. An exhaustive benchmark was performed both with and without solvent inclusion using a set of hybrid functionals (B3LYP, mPW1PBE, mPW3PBE, B3W91, B97, B972, B98, HSEh1PBE, PBEh1PBE) as well as the following basis sets: 6-31G*, 6-31G**, 6-31++**, 6-311G, 6-311G**, 6-311G++**, cc-pVDZ, SV, SVP, D95, D95 V, SHC, CEP-4G, CEP-31G, TZV, TZVP, Def2SV, Def2SVP, MidiX. On the basis of this work it was determined that B972/6-311G was the best pairing for experimental correlation. All the geometries correspond to equilibrium structures as verified through frequency calculations. In all cases, the structures were obtained in a vacuum and in chloroform, using the conductor-like polarizable continuum model (CPCM). The first 15 excited states and UV−vis simulations were computed through time-dependent density functional theory (TD-DFT) applied to the optimized ground state for each cruciform in chloroform. The HOMO, LUMO, and band gap energies were also calculated from these ground state optimizations. The first excited state, which is the HOMO−LUMO transition was used to derive the optical band gap.[26] Using GaussView6 software the UV−vis spectrum was simulated through a Gaussian curve fit to the TDDFT output.

Materials. Br-DAHQ (**1**),[27] polyphosphoric acid silyl ester (PPSE),[32,33] 2,6-diphenyl-4,8-dibromobenzobisoxzole[22,28] were synthesized according to literature procedures. Tetrahydrofuran (THF) and toluene were dried using an Innovative Technologies solvent purification system. All other chemical reagents were purchased from commercial sources and used without further purification unless otherwise noted.

Instrumentation. Nuclear magnetic resonance (NMR) experiments were carried out in $CDCl_3$ at 400 or 500 MHz (^1H), 101 MHz (^{13}C), and 470 MHz (^{19}F). In all spectra, chemical shifts are given in δ relative to tetramethylsilane. Coupling constants are reported in hertz (Hz). High resolution mass spectra were recorded on a double-focusing magnetic sector mass spectrometer using ESI. Melting points were obtained on a melting point apparatus with 300 °C upper limit and are uncorrected. The electrochemical data of the benzobisoxazoles small molecules were collected using a platinum working electrode, 0.1 M Bu_4NPF_6 in acetonitrile as the electrolyte, platinum wire for the auxiliary electrode, a Ag/Ag^+ reference electrode under an argon atmosphere and all recorded on an eDAQ e-corder 410. All solution UV−vis and fluorescence spectra were obtained using 5×10^{-6} M $CHCl_3$ solutions in 10 mm path length quartz cells unless otherwise noted. Film UV−vis spectra were obtained by spun-coated films of each molecule on 25 mm glass slides from solution concentrations of 5−10 mg/mL. The glass slides were first cleaned by 30 min sonications of distilled water, acetone, and finally 2-propanol. UV−vis spectra were collected on a Shimadzu UV-1800 UV spectrophotometer. Photolumines-

DOI: 10.1021/acs.jpca.8b07778
J. Phys. Chem. A 2019, 123, 1343−1352

cence spectra were obtained on a Varian Cary Eclipse spectrophotometer. Absolute solution fluorescence quantum yields were obtained using a HORIBA spectrophotometer Nanolog FL3-2iHR equipped with a Quanta-phi integrating sphere. Fluorescence lifetimes were carried out on a Life spec II spectrophotometer from Edinburgh Instruments, equipped with a 405 nm picosecond pulsed diode laser with vertical polarization.

General Cross-Coupling Procedure for SM 1−3 and SM 1-F−3-F via Suzuki Reaction. In a three-necked RBF purged with argon, fitted with a condenser, monomer **2** or **3** (0.25 mmol) and corresponding boronic ester (0.625 mmol) were dissolved in degassed toluene. One drop of Aliquot 336 (surfactant) was added to the reaction flask, followed by 2 M sodium carbonate (6 mL, 12 mmol). The reaction solution was then deoxygenated for 30 min by pumping argon through the solution. PEPPSI-*i*Pr catalyst (0.0125 mmol) was added and the reaction kept at reflux for 36 h under argon. The solution was then diluted with chloroform and deionized water to separate layers. Aqueous layers were extracted twice with chloroform (2 × 20 mL). The combined organic layers were washed with 1 M hydrochloric acid, water, and brine and dried with magnesium sulfate. After concentration, the residue was purified by column chromatography with silica gel (gradient hexanes to 50/50 v/v hexanes/dichloromethane). The eluents were concentrated and dissolved in 1.5−5 mL of chloroform and precipitated into cold methanol (−78 °C). The resulting powder was taken through a second column by dry packing to silica, following the same gradient, and then precipitated into methanol to yield the corresponding small molecules.

*4,8-Dibromo-2,6-bis(perfluorophenyl)benzo[1,2-d:4,5-d′]-bis(oxazole) (**2**).* In a dried round-bottomed flask (RBF), a fresh prepared solution of polyphosphoric acid silyl ester (PPSE)[29,30] (5g of P_2O_5, 10 mL of hexamethyldisiloxane in 20 mL of *o*-DCB, was kept at reflux for 1 h) and **1** were degassed for 20 min. Pentafluorobenzoyl chloride was added, and the solution was kept at reflux for 2 days under argon. The solution was allowed to cool to room temperature and precipitated into cold methanol (−78 °C). The precipitate was filtered and recrystallized from acetone to yield off-white needles (36%): mp 254 °C; ^{19}F NMR (470 MHz, $CDCl_3$) δ −135.08 (4F, d), −145.94 (2F, m), −159.37 (4F, dd). HRMS (ESI) calcd for $C_{20}Br_2F_{10}N_2O_2$: 648.8245 $[M + H]^+$. Found: 648.8245 theoretical.

*4,8-Bis(4-(tert-butyl)phenyl)-2,6-diphenylbenzo[1,2-d:4,5-d′]bis(oxazole) (**SM 1**).* **SM 1** was synthesized according to the general Suzuki procedure from **2** and **4**. The product was obtained as a white powder (80 mg, 55%): mp >300 °C; ^{1}H NMR (500 MHz, $CDCl_3$) δ 8.40 (4H, d, J = 10 Hz), 8.35 (4H, bs), 7.69 (4H, d, J = 5 Hz), 7.55 (6H, bs), 1.46 (18 H, s). HRMS (ESI) calcd for $C_{40}H_{36}N_2O_2$: 577.2855 $[M + H]^+$. Found: 577.2838.

4,8-Bis(4-(tert-butyl)phenyl)-2,6-bis(perfluorophenyl)-benzo[1,2-d:4,5-d′]bis(oxazole) (SM 1-F). SM 1-F was synthesized according to the general Suzuki procedure from **3** and **4**. The product was obtained as a light yellow powder (70 mg, 37%): mp >300 °C; ^{1} H NMR (500 MHz, $CDCl_3$) δ 8.34 (4H, d, J = 10 Hz), 7.65 (4H, d, J = 10 Hz), 1.42 (18H, s); ^{19}F (470 MHz, $CDCl_3$) δ −136.04 (4F, dd), −147.96 (2F, s), −160.06 (4F, dd). HRMS (ESI) calcd for $C_{40}H_{26}F_{10}N_2O_2$: 757.1913 $[M + H]^+$. Found: 757.1933.

4,8-Bis(9,9-dihexyl-9H-fluoren-2-yl)-2,6-diphenylbenzo-[1,2-d:4,5-d′]bis(oxazole) (SM 2). SM 2 was synthesized according to the general Suzuki procedure from **2** and **5**. The product was obtained as light-yellow flakes (128 mg, 57%): mp 215−216 °C; ^{1} H NMR (400 MHz, $CDCl_3$) δ 8.49 (2H,dd, J = 8, 4 Hz), 8.45 (s), 8.37 (m), 7.99 (d, J = 8 Hz), 7.84 (d, J = 8 Hz), 7.56 (d, J = 4 Hz), 7.42 (m), 2.15 (m), 1.13 (m), 0.95 (m), 0.75 (t, J = 8, 4 Hz); ^{13}C (101 MHz, $CDCl_3$) δ 164.00, 151.84, 151.21, 146.96, 141.61, 141.38, 138.95, 131.96, 131.66, 129.60, 129.32, 128.13, 127.85, 127.71, 127.33, 125.39, 123.47, 120.48, 120.27, 115.34, 55.70, 41.17, 32.04, 30.52, 24.49, 23.20, 14.46. HRMS (ESI) calcd for $C_{70}H_{76}N_2O_2$: 977.5985 $[M + H]^+$. Found: 977.5963.

4,8-Bis(9,9-dihexyl-9H-fluoren-2-yl)-2,6-bis-(perfluorophenyl)benzo[1,2-d:4,5-d′]bis(oxazole) (SM 2-F). SM 2-F was synthesized according to the general Suzuki procedure from **3** and **5**. The product was obtained as a yellow powder (127 mg, 44%): mp 109−111 °C; ^{1} H NMR (500 MHz, $CDCl_3$) δ 8.45 (4H, m), 7.95 (2H, d, J = 5 Hz), 7.79 (2H, dd, J = 10, 5 Hz), 7.41 (2H, m), 7.37 (4H, m), 2.09 (8H, m), 1.07 (28H, m), 0.81 (4H, m), 0.72 (12H, t, J = 15, 5 Hz); ^{19}F (470 MHz, $CDCl_3$) δ −135.91 (4F, s), −148.02 (2F, s), −160.07 (4F, s). HRMS (ESI) calcd for $C_{70}H_{66}F_{10}N_2O_2$: 1157.5043 $[M + H]^+$. Found: 1157.5027.

4,8-Bis(9-(heptadecan-9-yl)-9H-carbazol-3-yl)-2,6-diphenylbenzo[1,2-d:4,5-d′]bis(oxazole) (SM 3). SM 3 was synthesized according to the general Suzuki procedure from **2** and **6**. The product was obtained as a bright yellow powder (144.8 mg, 52%): mp 130−132 °C; ^{1} H NMR (400 MHz, $CDCl_3$) 9.29 (2H, d, J = 4 Hz), 8.64 (2H, m), 8.45 (4H, dd, J = 8, 4 Hz), 8.32 (2H, m), 7.87 (2H, d J = 8 Hz), 7.68 (2H, m), 7.58 (6H, m), 7.52 (4H, m), 7.32 (2H, m), 4.69 (2H), 2.42 (4H, m), 2.03 (4H, m), 1.22 (48H, m) 0.84 (12H, t, J = 12, 4 Hz); ^{13}C (101 MHz, $CDCl_3$) δ 163.51, 146.53, 138.37, 131.34, 128.88, 128.00, 127.79, 127.53, 125.72, 125.31, 124.27, 123.07, 122.43, 122.19, 120.63, 120.31, 118.79, 114.52, 111.67, 108.91, 56.54, 33.92, 31.79, 29.51, 29.38, 29.23, 26.94, 22.61, 14.06. HRMS (ESI) calcd for $C_{78}H_{94}N_4O_2$: 1119.7455 $[M + H]^+$. Found: 1119.7479.

4,8-Bis(9-(heptadecan-9-yl)-9H-carbazol-3-yl)-2,6-bis-(perfluorophenyl)benzo[1,2-d:4,5-d′]bis(oxazole) (SM 3-F). SM 3-F was synthesized according to the general Suzuki procedure from **3** and **6**. The product was obtained as an orange-yellow powder (113.3 mg, 35%): mp 216−218 °C; ^{1} H NMR (500 MHz, $CDCl_3$) 8.60 (2H, d, J = 10 Hz), 8.14 (2H, dd, J = 15, 5 Hz), 7.87 (2H, d, J = 30, 5 Hz), 7.56 (2H, d, J = 5 Hz) 7.39 (2H, d, J = 10 Hz), 7.22 (2H, m), 4.56 (2H, bs), 2.28 (4H, m), 1.89 (4H, m), 1.13 (44H, m), 0.97 (4H, m), 0.81 (12H, t, J = 10, 5 Hz); ^{19}F (470 MHz, $CDCl_3$) δ −135.08 (4F, m), −145.93 (2F, m), −159.36 (4F, m). HRMS (ESI) calcd for $C_{78}H_{84}F_{10}N_4O_2$: 1299.6513 $[M + H]^+$. Found: 1299.6503

UPS Process and Characterization. Ultraviolet photoelectron spectroscopy (UPS) was used to acquire the ionization potentials to approximate the HOMO values for each small molecule. All substrates (positively doped silicon; 10 × 10 mm^2) had 40 nm of silver deposited via thermal evaporation. Samples were prepared by dissolution in chloroform at concentrations of 5 and 2.5 mg/mL and stirred for a minimum of 4 h. Each sample was first filtered to remove potential aggregates and sequentially spin-coated under a nitrogen atmosphere at 2000 and 4000 rpm (2.5 mg/mL was only spun at 4000 rpm). Spectra were then acquired under ultrahigh vacuum. The presented HOMO energies and corresponding standard deviations are determined by using all values obtained at random positions.

DOI: 10.1021/acs.jpca.8b07778
J. Phys. Chem. A 2019, 123, 1343−1352

Scheme 1. Synthetic Route for BBOs 1−3, 1F−3F

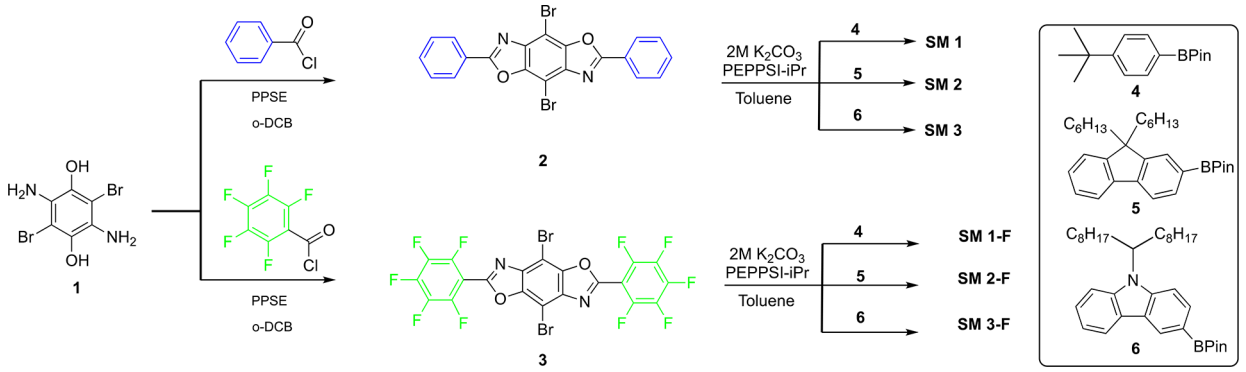

RESULTS AND DISCUSSION

Molecular Synthesis and Characterization. The synthetic approach for the BBO small molecules is shown in Scheme 1. The small molecules were made using our traditional approach in which the aryl substituent along the 2,6-axis is introduced via condensation of 3,6-diamino-2,5-dibromohydroquinone (**1**) with either benzoyl chloride or pentafluorobenzoyl chloride to afford compounds **2** and **3** with yields of 48% and 36%, respectively. In our previous work, compound **2** was obtained in very low yield (23%).[28] In this instance we were able to increase the yield by refluxing the crude product in ethanol to remove 2,5-diamino-3,6-dibromocyclohexa-2,5-diene-1,4-dione from the fairly insoluble product **2**. The perfluorophenyl substituted product, **3**, can be recrystallized from acetone due to its polar nature and good solubility. The low yields of the BBO synthons is a result of the extreme temperatures needed to drive the condensation reaction forward (180 °C), which can cause the decomposition of **1**. Additionally, the water produced from the reaction can hydrolyze the acid chlorides, further decreasing yields. The second step of the synthesis is the Suzuki cross-coupling reaction of **2** and **3** with the boronic esters **4**, **5**, or **6** to generate **SM 1−6**. Each molecule was treated with a standard work up followed by purification via column chromatography to remove residual catalyst, unreacted boronic ester, and/or remaining deborylated arene. A subsequent column and precipitation into methanol at −78 °C was employed to further purify the molecules. Small molecules **3−6** were soluble in chlorinated solvents while **SM 1** and **SM 1-F** had limited solubility. The structures of the molecules were confirmed using ^{1}H nuclear magnetic resonance (NMR) spectroscopy and high resolution mass spectrometry (HRMS). Due to the large number of fluorine atoms, lack of a two-channel decoupler, and/or limited solubility, ^{13}C NMR spectroscopy was not performed on **SM 1**, **SM 1-F**, **SM 2-F**, and **SM 3-F**. The thermal properties were studied using thermogravimetric analysis under nitrogen at a heating rate of 10 °C. Each small molecule showed high thermal stability with the 5% weight loss temperatures ranging from 228 to 396 °C, as shown in Figures S2 and S3. Interestingly, the nonfluorinated BBOs had good thermal stability while the fluorinated BBOs had decomposition temperatures that were on average 100 deg lower. Nonetheless, all materials are stable enough for potential use in OLED or OPV applications.

Experimental and Theoretical Optical Properties. The photoluminescence spectra of the BBO cruciforms in solution are shown in Figure 1, and the thin film emission spectra are

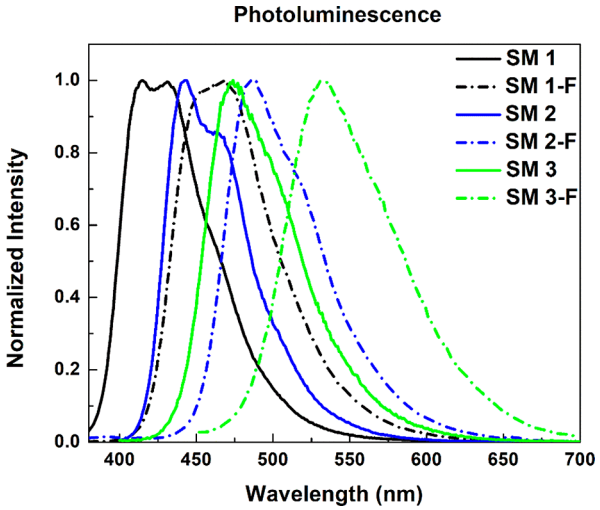

Figure 1. Solution photoluminescence plots of SM 1 to SM 3-F in chloroform.

shown in Figure S5. The data are summarized in Table 1. The influence of aryl group substitution can be evaluated by examining the emission spectra for the respective phenyl (**SM 1**, **SM 2**, and **SM 3**) and perfluorophenyl (**SM 1-F**, **SM 2-F**, and **SM 3-F**) families. The phenyl substituted BBOs **SM 1** and **SM 2** both exhibited blue emission, with **SM 2** exhibiting a bathochromic shift of 15 nm. This observation is a result of the increased conjugation length of the fluorenyl substituents along the 4,8-axis of **SM 2** versus the phenyl substituents along the same axis of **SM 1**. The emission for **SM 3** was red-shifted relative to both **SM 1** and **SM 2** due to the greater donor strength of the carbazoyl group, which increased charge transfer. The emission maxima for the perfluorophenyl BBOs **SM 1-F**, **SM 2-F**, and **SM 3-F** were all red-shifted by an average of 45 nm from their analogous phenyl substituted BBOs. This is a result of the enhancement of the CT character of the excited state, due to the increase of the spatial separation of the HOMO and LUMO, as shown in Figure 5. The quantum yields for all of the small molecules are given in Table 1. In each case, the perfluorophenyl substituted BBOs **SM 1-F**, **SM 2-F**, and **SM 3-F** had lower quantum yields in comparison to their phenyl counterparts. The fluorine substitution also caused an overall decrease in both the absorption and radiative decay. As seen in Table 1, the molar absorptivity decreased upon fluorination, which caused a decrease in the rate of radiative decay in each set of the molecules while maintaining little to no change in the rate of nonradiative decay, as shown

DOI: 10.1021/acs.jpca.8b07778
J. Phys. Chem. A 2019, 123, 1343−1352

Table 1. Optical and Electronic Properties for BBO Cruciforms and Predicted Excited States[a]

	solution						DFT excited states								film	
			E_g^{opt} (eV)													
BBO	Φ	λ_{max}^{Em}(nm)	expt	DFT	λ_{max}^{abs} (nm)	ε (M^{-1} cm^{-1})	λ_1 (nm)	f	λ_2 (nm)	f	λ_3 (nm)	f	λ_4 (nm)	f	λ_{max}^{abs} (nm)	λ_{max}^{Em} (nm)
SM 1	31	430	2.90	3.03	293, **356**	47800	385	0.69	**342**	1.09	291	0.91			355	438
SM 1-F	25	445	2.70	2.91	287, **339**	33600	426	0.39	321	0.67	317	0.43	**300**	0.99	354	487
SM 2	72	443	2.70	2.96	273, 329, **364**	62400	419	0.96	349	1.07	**327**	1.16			335	471
SM 2-F	37	486	2.50	2.56	**329**, 426	55800	485	0.59	**344**	1.39	331	0.50	328	0.46	330	513
SM 3	42	473	2.60	2.83	270, **304**, 342, 357, 397	61600	437	0.49	**344**	1.23	313	0.49	309	0.54	346	486
SM 3-F	33	535	2.30	2.38	275, **322**, 418	59000	521	0.34	**334**	1.01	322	0.60	322	0.35	460	531

[a]Only those DFT states for which the oscillator strength was deemed significant ($f \geq 0.34$) were recorded. The experimental peak maxima, and highest oscillator strengths are bolded.

in Figure S7. The perfluorophenyl-based BBOs also exhibited drastically longer fluorescence lifetimes, nearly double in each case. The increased lifetime echoes our previous statement on the increased CT state especially in the case of the 3--linked carbazole molecules (**SM 3**, **SM 3-F**). The direct conjugation of the nitrogen in combination with the more spatially segregated LUMO allows for more efficient ICT, which is seen by electro-optical data in Table 1 and is supported by the calculated oscillator strengths for each series, a phenomenon that is not ideal for OLEDs but may benefit OPV materials.[31]

The solution UV−vis spectra of the BBO cruciforms in chloroform are shown in Figure 2 and are plotted with their

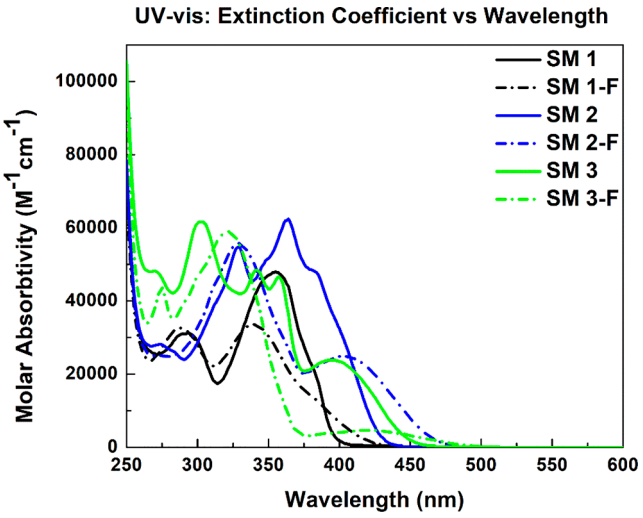

Figure 2. Solution UV−vis plots of SM 1 to SM 3-F in chloroform.

simulated counterparts in Figure 3. The thin film absorption spectra are shown in Figure S4. The experimental data are summarized in Table 1 along with the computational results. Overall, the calculated peak maxima show a good match (~40 nm) to the experimental values. The influence of fluorination can be evaluated by examining the absorbance spectra for the respective phenyl and perfluorophenyl pairs (**SM 1**/**SM 1-F**, **SM 2**/**SM 2-F**, and **SM 3**/**SM 3-F**) as well as their families. We will begin by looking at each system by discussing pair differences in which only those simulated excited states with oscillator strengths (f) of 0.34 or higher will be compared to experimental spectra.

In the case of **SM 1**, there are three excited states that adhere to the criteria stated above: 385.10 nm (f = 0.69), 342.22 nm (f = 1.09), and 291.64 nm (f = 0.91). The simulated spectrum that takes these as well as the other lowest 15 excited states (see Figure S24) predicts peaks at 350 and 299 nm, which are quite close to the experimental values of 356 and 293 nm, respectively. For **SM 1-F**, four excited states are found to be significant contributors to the simulated spectrum where three (321.4, 317.4, and 300.8 nm) led to a single intense peak and the fourth is a broad low energy peak centered around 426.6 nm. The experimental spectrum, however, shows two peaks of nearly equal intensity where one is at 287 nm and a second with a shoulder at 339 nm. When compared to the predicted excited states, there is a 13.3 nm difference between the higher energy peaks and a 20 nm difference between the experimental lower energy peak and the averages of the 321 and 317 nm excited states. The experimental spectra for **SM 1** and **SM 1-F** possess nearly identical high energy bands, but the intensity and profile of the lower energy peaks differ (Figure S23). These results indicate that the higher energy states are more influenced by the aryl substituents along the 4,8-axis for this set of cruciforms and the inclusion of the five fluorine atoms leads to a blue shift and a repression of absorptivity for the lower energy peak.

In the case of **SM 2**, there are three excited states that adhere to the criteria stated above in which the two largest (327 and 349 nm) are quite close to the experimental peaks (329 and 364 nm). However, the third excited state at 419 nm is a shoulder in the simulated spectra and is absent from the experimental spectra. For **SM 2-F**, the simulated spectrum displays a peak maximum around 338 nm, which is less than 10 nm from the 329 nm experimental peak. The computed excited states indicate this 338 nm peak is produced from three excited states (344.7, 331.2, and 328.3 nm). Additionally, there was a less intense broad peak around 485 nm (f = 0.59 versus f = 1.39 for λ_{max}), which is red-shifted and less intense than the higher energy peak seen in the experimental spectrum at 426 nm. Similar to the case for the **SM 1** and **SM 1-F** pair, both **SM 2** and **SM 2-F** possess a similar high energy peak and share the same 329 nm wavelength maximum. With regard to their lower energy peaks, **SM 2** and **SM 2-F** differ for both experimental and simulated spectra where, again, inclusion of the perfluorophenyl group results in a blue-shifted peak.

In the case of **SM 3**, there are three excited states with significant oscillator strengths (344.0, 313.8, and 309.1 nm) that contribute to the predicted spectral maximum at ~323 nm. The simulated spectrum also displays a lower energy shoulder at 437 nm, which is consistent with the low energy peak in the experimental version, although the latter is much

DOI: 10.1021/acs.jpca.8b07778
J. Phys. Chem. A 2019, 123, 1343−1352

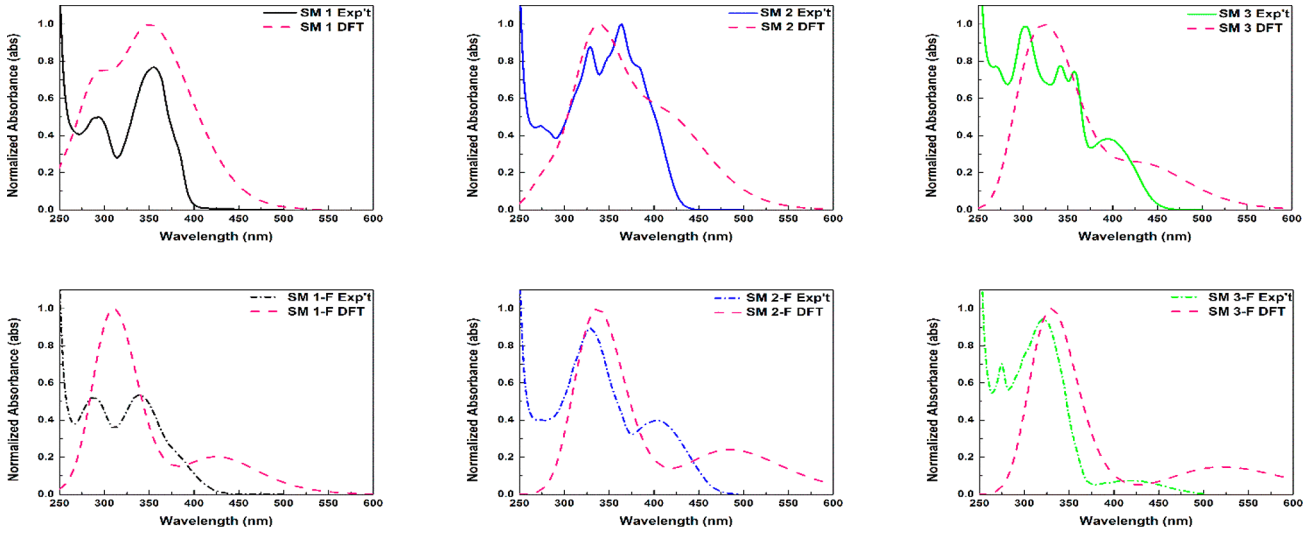

Figure 3. Comparison of the simulated and experimental UV−vis spectra of **SM 1 to SM 3-F** in chloroform.

more red-shifted. The experimental spectrum has a high energy shoulder (270 nm) as well as three distinct peaks (304, 342, and 357 nm) and a broad low energy peak at 397 nm. Finally, for **SM 3-F** the simulated spectrum predicted a peak maximum at 331 nm, which was only 9 nm different from the experimental value. This peak is generated from three excited states (334.9, 322.5, and 322.1 nm). Additionally, a low broad peak is predicted at 521.8 nm. The experimental UV−vis spectrum has two peaks: one small, high energy peak at 275 nm and an intense peak at 322 nm. Moreover, there was one weak and broad peak at 418.5 nm, although significantly blue-shifted compared to the simulated spectrum, is nonetheless, consistent with overall spectral trends. Unlike the previous pairs, there is a lack of similarity between the high energy peaks for **SM 3** and **SM 3-F** in the experimental spectra. This result is likely due to the structural differences of **SM 3** and **SM 3-F** relative to the other cruciforms. Due to the connection at the 3-position of the carbazole, these molecules are conjugated through the nitrogen atoms instead of carbon like the others.

An analysis of the families provided an insight on the impact of aryl substitution along the 4,8-axis on the UV−vis spectra. For both families, the absorption spectra were affected by conjugation length and a bathochromic shift was observed for the fluorene substituted BBOs. The simulated absorption spectra for the phenyl substituted BBOs, **SM 1**, **SM 2**, and **SM 3**, all differed in peak band structures, Figure S30. Conversely, the simulated absorption for the fluorinated family, **SM 1-F**, **SM 2-F**, and **SM 3-F**, all featured a strong, higher energy peak and a smaller low energy peak, Figure S32. This indicates that the chromophore resulting from the pentafluorobenzene group is responsible for the high energy peak. We are also able to see the similar trends between conjugation length and absorption spectra within the experimental data for the perfluorophenyl substituted BBOs. Unfortunately, the morphology of the peaks within the experimental spectra for the phenyl family differs dramatically from the theoretical results, making comparisons between the series challenging. We believe this to be a result of contributions from different chromophores arising from the various conformations these structures can adopt in combination with the vibronic coupling for specific transitions within the cruciforms.[22] Thus, while several aspects of the absorption spectra can be predicted, the possibility for multiple conformations makes it difficult to predict the complete spectrum for the small molecules.

To further elucidate the origins of the peaks in the simulated UV−vis spectra, a detailed examination of the molecular orbitals, which gave rise to each transition for the excited states possessing oscillator strengths of 0.34 or greater, was performed. The details of this study are given in the Supporting Information and summarized in Table 2. The

Table 2. Transition Types (ICT versus LE) of the BBO Cruciforms[a]

	ES		ES		ES		ES	
BBO	*f*	type	*f*	type	*f*	type	*f*	type
SM 1	0.69	LE	1.09	LE	0.91	LE		
SM 1-F	0.39	ICT	0.67	ICT	0.43	ICT	0.99	LE
SM 2	0.96	ICT	1.07	LE	1.16	LE		
SM 2-F	0.59	ICT	1.39	LE	0.50	ICT	0.46	ICT
SM 3	0.49	ICT	0.49	LE	1.23	LE	0.54	LE
SM 3-F	0.34	ICT	1.01	LE	0.60	LE	0.35	ICT

[a]For predicted excited states with ($f \geq 0.34$)of the BBO cruciforms.

nature of the transitions are categorized as either intramolecular charge transfer (ICT) or local excitation (LE). ICT is defined as a significant redistribution of electron density from one location within a molecule to another, whereas a lack of redistribution within the molecule is indicative of LE. In the case of the **SM 1**/**SM 1-F** pair, we see a change in transition type from LE to ICT, which is due to a reduction in the symmetry of molecule. For the other BBO pairs, perfluorination does not change the nature of the transition type for each significant excited state and hence there was no clear pattern observed.

Experimental and Theoretical Electrochemical Properties. The experimental band gaps of **SM 1 to SM 3-F** were determined two ways: from the onset on the absorption spectra (Table 1) and via cyclic voltammetry (CV) (Table 3). The redox graphs are located in the Supporting Information. Although the absolute values varied based on the technique used, they were within the typical margin of error expected.[32] The trends in the size of the band gaps within families **SM 3** <

DOI: 10.1021/acs.jpca.8b07778
J. Phys. Chem. A 2019, 123, 1343−1352

Table 3. Electronic Properties and Dihedral Angles of the BBO Cruciforms

	gas phase (UPS)				chloroform (CF)					
	HOMO[a] (eV)		dihedral angle (deg)		HOMO[b] (eV)		LUMO[c] (eV)	E_g^{EC} (eV)	dihedral angle (deg)	
BBO	expt[c]	DFT	4,8-axis	2,6-axis	expt[b]	DFT	expt	expt	4,8-axis	2,6-axis
SM 1	−5.9	−5.66	148.2	175.8	−6.0	−5.91	−3.3	2.7	144.2	178.2
SM 1-F	−5.9	−6.06	152.7	139.4	−6.2	−6.14	−3.3	2.9	147.4	138.3
SM 2	−5.7	−5.48	147.7	174.8	−5.7	−5.71	−3.2	2.5	144.3	177.4
SM 2-F	−5.9	−5.74	152.6	142.1	−5.8	−5.84	−3.2	2.6	148.2	142.7
SM 3	−5.4	−5.23	149.7	175.0	−5.5	−5.47	−3.3	2.2	145.4	178.2
SM 3-F	−5.4	−5.47	155.1	142.7	−5.6	−5.58	−3.3	2.3	150.3	142.9

[a]Determined by UPS spectroscopy. [b]HOMO = $-(E_{onset}^{ox} + 4.8)$ eV. [c]LUMO = $-(E_{onset}^{red} + 4.8)$ eV. The electrochemical data of the benzobisoxazoles was collected using a platinum working electrode, acetonitrile, and 0.1 M Bu_4NPF_6 as the electrolyte and a Ag/Ag^+ reference electrode under an argon atmosphere.

SM 2 < **SM 1** and **SM 3-F** < **SM 2-F** < **SM 1-F** were also consistent.

Within the BBO pairs, the optical band gaps for the fluorinated BBOs were smaller than the analogous phenyl derivatives (Chart 3). There was an absolute difference of 0.26

Chart 3. Band Diagram for the DFT Computations in Chloroform Where the Lower Value Is the HOMO Level, the Upper Value Is the LUMO Level, and the Optical Band Gap (Determined from the First Excited State) Is in the Middle[a]

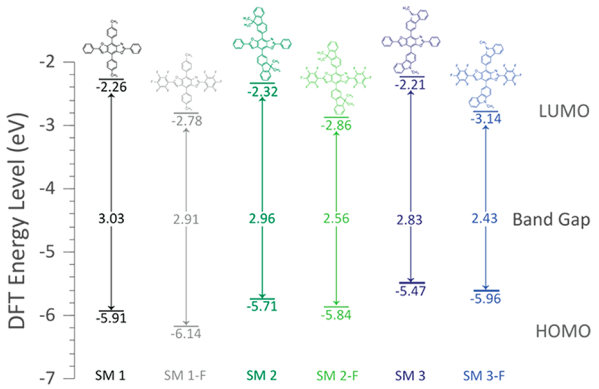

[a]In each case the structure of the corresponding cruciform is given for clarity.

eV or less between the experimentally determined optical band gaps and the theoretical band gaps. However, the electrochemical data indicated an opposite trend in which the fluorinated BBOs had slightly larger bandgaps (E_g^{EC}) than the analogous phenyl derivatives. Although the small molecules each showed reversible oxidation and reduction processes, the LUMO measurement was difficult to determine, as evidenced by the voltammogram shape of the reduction cycle. This contributes to error in the LUMO measurement and also impacts the band gap. For this reason, we also characterized the small molecules via UPS, which provided an absolute determination of the ionization potential, which can be correlated to the HOMO level.[33−35] The data obtained from UPS confirm our hypothesis that changes along the 2,6-axis had nominal impact on the position of the HOMO level as both the **SM 1** **SM 1-F** and **SM 3**/**SM 3-F** pairs have the same values, Table 3. In the case of the **SM 2**/**SM 2-F** pair, a small change is seen that was likely a result of the extended conjugation along the 4,8-axis.

This trend was not seen in gas phase calculation where the electron-withdrawing nature of the fluorine was predicted to have a significant impact on the HOMO level. Regardless of medium, calculations indicate that the fluorinated systems had deeper HOMO energies than their nonfluorinated counterparts. There was excellent comparison between the theoretical determinations in chloroform and the CV measurements with a maximum absolute difference of 0.09 eV. The trend for the HOMO level depth within families is **SM 3** < **SM 2** < **SM 1** and **SM 3-F** < **SM 2-F** < **SM 1-F**. This trend is due to an increase in conjugation for **SM 1** vs **SM 2** and **SM 1-F** vs **SM 2-F** and an increase in both conjugation and donor behavior for **SM 1** vs **SM 3** and **SM 1-F** vs **SM 3-F**. These findings are supported by the dihedral angle study and FMOs discussed below.

Optimized ground state geometries of the BBO's cruciforms were obtained through density functional theory (DFT), and the dihedral angles are defined in Figure 4. The data are

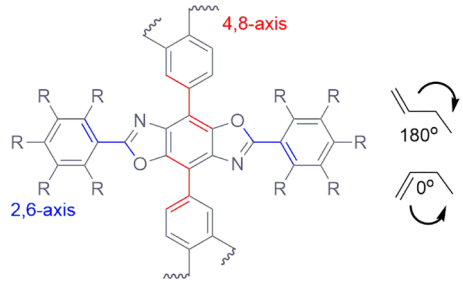

Figure 4. Dihedral angle definitions for BBO cruciforms.

summarized in Table 3 and provide an indication of conjugation length within the BBOs. Cruciforms in which the dihedral angle is closer to 180° indicate that the system is more planar, thereby facilitating π-delocalization. Regardless of the medium, within the BBO pairs, the dihedral angles along the 4,8-axis of the perfluorophenyl BBOs are more planar than their phenyl analogues. Conversely, the dihedral angles along the 2,6-axis of the perfluorophenyl BBOs are less planar than their phenyl analogs. For each family, the order of planarity in the gas phase along the 4,8-axis is **SM 3** > **SM 1** > **SM 2** and **SM 3-F** > **SM 1-F** ∼ **SM 2-F**, which is mirrored by the chloroform results with the exceptions being **SM 2-F** and **SM 1-F**. This difference in the dihedral angles of **SM 2-F** and **SM 1-F** may be a result of the increased size of the fluorenyl group. There was no clear trend in the 2,6-axis dihedral angle within the families.

DOI: 10.1021/acs.jpca.8b07778
J. Phys. Chem. A 2019, 123, 1343−1352

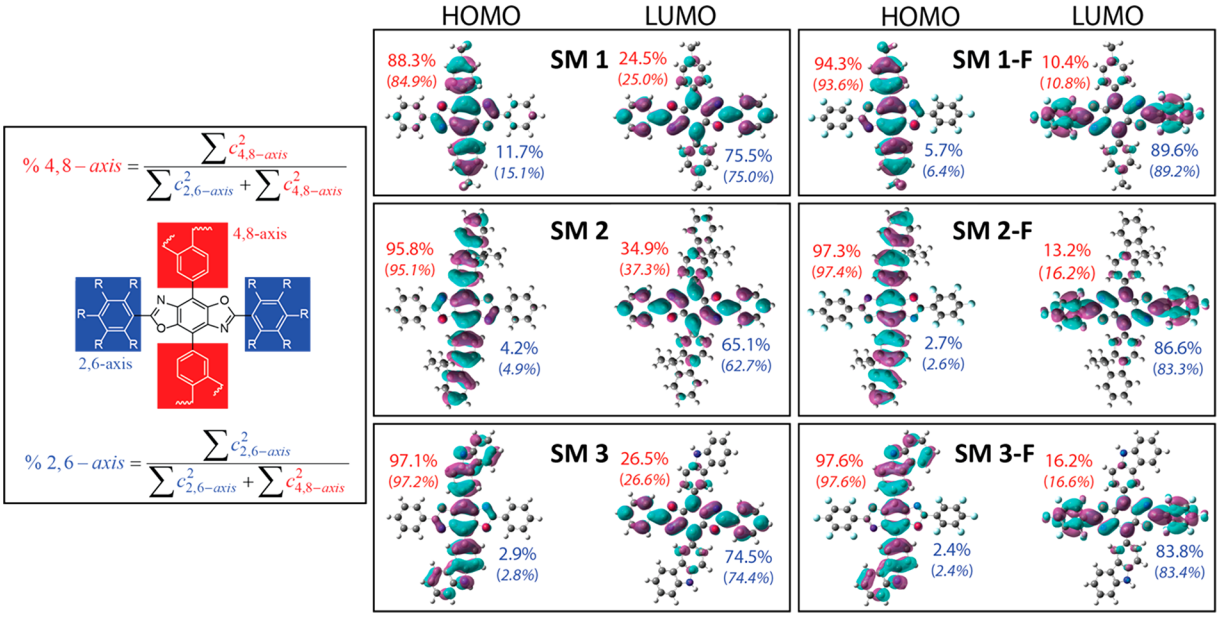

Figure 5. Frontier molecular orbitals for all materials in which the percentages determined in vacuum are in red for the 4,8- and blue for the 2,6-axes. Those in parentheses are for percentages determined in chloroform. The values were obtained using the formula on the left.

The FMO charge distributions for the optimized structures are shown in Figure 5, along with the calculated percentages of electron density along each axis.[22] Overall, there were higher percentages of localization of the HOMO along the 4,8-axis and the LUMO along the 2,6-axis. Within the cruciforms pairs, the perfluorophenyl BBOs had significantly higher percentages of localization along the 2,6-axis and slightly higher localization along the 4,8-axis than the phenyl analogs. This observed increase in localization of electron density further supports our theory that, within systems that demonstrate donor−acceptor behavior, the substituents along the 2,6-axis greatly impact the LUMO while nominally impacting the HOMO. Within the BBO families, the localization of the electron density in the HOMO increases as a function of the conjugation length of the aryl group along the 4,8-axis (**SM 3** > **SM 2** > **SM 1** and **SM 3-F** > **SM 2-F** > **SM 1-F**), regardless of medium used (gas or chloroform). The opposite effect was seen for the LUMO of the perfluorophenyl series since the electron density decreases as a function of the conjugation length of the aryl group along the 4,8-axis (**SM 1-F** > **SM 2-F** > **SM 3-F**). For the cruciform pairs, the electron density within both the HOMO and LUMO is more localized for the pentafluorobenzene substituted BBOs than the phenyl substituted BBOs **SM 1-F** > **SM 1**, **SM 2-F** > **SM 2** and **SM 3-F** > **SM 3**. The data also validated the trends in the HOMO energies and band gaps discussed previously.

CONCLUSIONS

We synthesized, characterized, and modeled a set of cross-conjugated materials based on a benzo[1,2-*d*:4,5-*d*′] bisoxazole moiety bearing phenyl, fluorenyl, and carboxyl aryl groups along the 4,8-axis and either phenyl or perfluorophenyl along the 2,6-axis. The simulated model was found to be well-matched to the experimental optical and electronic data. Furthermore, all of the data support the notion that the cruciform architecture of the BBOs provides a tunable platform as changes along the 2,6-axis have only nominal impact on the HOMO levels. The perfluorophenyl substituents were also found to reduce the band gaps, which was consistent with the localization (higher percentage) of the electron density along the 4,8-axis for the HOMO and the 2,6-axis for the LUMO. Unfortunately, the perfluorophenyl materials had lower quantum yields than the phenyl analogs and their emissions were found to be more green than blue, thereby making them unusable in OLEDs. However, the band gap reduction that resulted from inclusion of an electron-withdrawing group along the 2,6-axis may be utilized as a design principle in the future for materials that require a smaller band gap (e.g., OPVs).

ASSOCIATED CONTENT

Supporting Information

The Supporting Information is available free of charge on the ACS Publications website at DOI: 10.1021/acs.jpca.8b07778.

Synthesis, characterization data (TGA, photoluminescence, CV, fluorescence lifetime plots/decay rates, NMR spectra), comparison of experimental vs simulated UV−vis spectra (PDF)

Theorical data, including Cartesian coordinates for gas and chloroform states, energy levels, tables of excited states, and local excitations vs intramolecular charge transfer from the MO transitions (PDF)

AUTHOR INFORMATION

Corresponding Authors

*E-mail: Aimee.Tomlinson@ung.edu.
*E-mail: malikaj@bu.edu.

ORCID

Malika Jeffries-EL: 0000-0002-9134-4938

Notes

The authors declare no competing financial interest.

ACKNOWLEDGMENTS

We thank Dr. Norman Lee, Stephon Betts, and Dr. Paul Ralifo from the Chemical Instrumentation Facility at Boston University for compound analysis. We also thank Margaret Chern from the Dennis Lab at Boston University for assistance

DOI: 10.1021/acs.jpca.8b07778
J. Phys. Chem. A 2019, 123, 1343−1352

in obtaining fluorescence lifetimes and quantum yields. Next, we thank Volodimyr Duzhko at the Center for Electronic Materials and Devices at the University of Massachusetts—Amherst. We also thank the National Science Foundation (CHE-141373, CHE-1640298, and CHE-1413207) as well a supercomputer allocation by the Extreme Science and Engineering Discovery Environment (XSEDE) for the Comet supercomputer cluster provided by the San Diego Supercomputing Center (DMR-160146) for supporting this work.

REFERENCES

(1) Wilson, J. N.; Josowicz, M.; Wang, Y.; Bunz, U. H. F. Cruciform π-Systems: Hybrid Phenylene-Ethynylene/Phenylene-Vinylene Oligomers. *Chem. Commun.* **2003**, 2962−2963.
(2) Klare, J. E.; Tulevski, G. S.; Sugo, K.; de Picciotto, A.; White, K. A.; Nuckolls, C. Cruciform p-Systems for Molecular Electronics Applications. *J. Am. Chem. Soc.* **2003**, *125*, 6030−6031.
(3) Wang, Z. J.; Liu, Z. T.; Gao, Z. H.; Yang, S. F.; Wang, Y. C.; Zhang, G. X.; Zhao, Y. S.; Zhang, D. Q. A New Benzodithiophene-Based Cruciform Electron-Donor-Electron-Acceptor Molecule with Ambipolar/Photoresponsive Semiconducting and Red-Light-Emissive Properties. *Asian J. Org. Chem.* **2017**, *6*, 1277−1284.
(4) Le, H. T. M.; El-Hamdi, N. S.; Miljanić, O. Š. Benzobisimidazole Cruciform Fluorophores. *J. Org. Chem.* **2015**, *80*, 5210−5217.
(5) Jo, M.; Lim, J.; Miljanić, O. Š. Selective and Sensitive Fluoride Detection through Alkyne Cruciform Desilylation. *Org. Lett.* **2013**, *15*, 3518−3521.
(6) Lim, J.; Nam, D.; Miljanic, O. S. Identification of Carboxylic and Organoboronic Acids and Phenols With a Single Benzobisoxazole Fluorophore. *Chem. Sci.* **2012**, *3*, 559−563.
(7) Spitler, E. L.; Shirtcliff, L. D.; Haley, M. M. Systematic Structure−Property Investigations and Ion-Sensing Studies of Pyridine-Derivatized Donor/Acceptor Tetrakis(arylethynyl)benzenes. *J. Org. Chem.* **2007**, *72*, 86−96.
(8) Jiang, S.; Lu, X.; Zhou, G.; Wang, Z.-S. Charge Transfer in Cross Conjugated 4,8-dithienylbenzo[1,2-b:4,5-b']dithiophene Based Organic Sensitizers. *Chem. Commun.* **2013**, *49*, 3899−3901.
(9) Havinga, E. E.; ten Hoeve, W.; Wynberg, H. Alternate Donor-Acceptor Small-Band-Gap Semiconducting Polymers; Polysquaraines and Polycroconaines. *Synth. Met.* **1993**, *55*, 299−306.
(10) van Mullekom, H. A. M.; Vekemans, J. A. J. M.; Havinga, E. E.; Meijer, E. W. Developments in the Chemistry and Band Gap Engineering of Donor-Acceptor Substituted Conjugated Polymers. *Mater. Sci. Eng., R* **2001**, *32*, 1−40.
(11) Chen, J.; Cao, Y. Development of Novel Conjugated Donor Polymers for High-Efficiency Bulk-Heterojunction Photovoltaic Devices. *Acc. Chem. Res.* **2009**, *42*, 1709−1718.
(12) Sakamoto, Y.; Suzuki, T.; Kobayashi, M.; Gao, Y.; Fukai, Y.; Inoue, Y.; Sato, F.; Tokito, S. Perfluoropentacene: High-Performance p−n Junctions and Complementary Circuits with Pentacene. *J. Am. Chem. Soc.* **2004**, *126*, 8138−8140.
(13) Sakamoto, Y.; Suzuki, T. Perfluorinated and Half-Fluorinated Rubrenes: Synthesis and Crystal Packing Arrangements. *J. Org. Chem.* **2017**, *82*, 8111−8116.
(14) Milián-Medina, B.; Gierschner, J. Though It Be but Little, It Is Fierce": Excited State Engineering of Conjugated Organic Materials by Fluorination. *J. Phys. Chem. Lett.* **2017**, *8*, 91−101.
(15) Battaglia, M. R.; Buckingham, A. D.; Williams, J. H. The Electric Quadrupole Moments of Benzene and Hexafluorobenzene. *Chem. Phys. Lett.* **1981**, *78*, 421−423.
(16) Chen, Z.; Zhang, W.; Huang, J.; Gao, D.; Wei, C.; Lin, Z.; Wang, L.; Yu, G. Fluorinated Dithienylethene−Naphthalenediimide Copolymers for High-Mobility n-Channel Field-Effect Transistors. *Macromolecules* **2017**, *50*, 6098−6107.
(17) Tang, M. L.; Bao, Z. Halogenated Materials as Organic Semiconductors. *Chem. Mater.* **2011**, *23*, 446−455.
(18) Calzolari, A.; Vercelli, B.; Ruini, A.; Virgili, T.; Pasini, M. Fluorine-Induced Enhancement of the Oxidation Stability and Deep-Blue Optical Activity in Conductive Polyfluorene Derivatives. *J. Phys. Chem. C* **2013**, *117*, 26760−26767.
(19) Osuna, R. M.; Ortiz, R. P.; Ruiz Delgado, M. C.; Sakamoto, Y.; Suzuki, T.; Hernández, V.; López Navarrete, J. T. Synthesis and Characterization of Three Novel Perfluoro-oligothiophenes Ranging in Length from the Trimer to the Pentamer. *J. Phys. Chem. B* **2005**, *109*, 20737−20745.
(20) Tlach, B. C.; Tomlinson, A. L.; Bhuwalka, A.; Jeffries-El, M. Tuning the Optical and Electronic Properties of 4,8-Disubstituted Benzobisoxazoles via Alkyne Substitution. *J. Org. Chem.* **2011**, *76*, 8670−8681.
(21) Tlach, B. C.; Tomlinson, A. L.; Morgan, K. D.; Collins, C. R.; Zenner, M. D.; Jeffries-El, M. Effect of Extended Conjugation on the Optoelectronic Properties of Benzo[1,2-d:4,5-d']bisoxazole Polymers. *Aust. J. Chem.* **2014**, *67*, 711−721.
(22) Tlach, B. C.; Tomlinson, A. L.; Ryno, A. G.; Knoble, D. D.; Drochner, D. L.; Krager, K. J.; Jeffries-El, M. Influence of Conjugation Axis on the Optical and Electronic Properties of Aryl-Substituted Benzobisoxazoles. *J. Org. Chem.* **2013**, *78*, 6570−6581.
(23) Lim, J.; Albright, T. A.; Martin, B. R.; Miljanić, O. Š. Benzobisoxazole Cruciforms: Heterocyclic Fluorophores with Spatially Separated Frontier Molecular Orbitals. *J. Org. Chem.* **2011**, *76*, 10207−10219.
(24) Saeed, M. A.; Le, H. T. M.; Miljanić, O. Š. Benzobisoxazole Cruciforms as Fluorescent Sensors. *Acc. Chem. Res.* **2014**, *47*, 2074−2083.
(25) Frisch, M. J.; Trucks, G. W.; Schlegel, H. B.; Scuseria, G. E.; Robb, M. A. C. J. R.; Montgomery, J. A., Jr.; Vreven, T.; Kudin, K. N.; Pople, J. A.; et al. *Gaussian 09*; Gaussian, Inc.: Wallingford, CT, 2009.
(26) Milian Medina, B.; VanVooren, A.; Brocorens, P.; Gierschner, J.; Shkunov, M.; Heeney, M.; McCulloch, I.; Lazzaroni, R.; Cornil, J. Electronic Structure and Charge-Transport Properties of Polythiophene Chains Containing Thienothiophene Units: A Joint Experimental and Theoretical Study. *Chem. Mater.* **2007**, *19*, 4949−4956.
(27) Heqedus, L. S.; Odle, R. R.; Winton, P. M.; Weider, P. R. Synthesis of 2,5-Disubstituted 3,6-Diamino-1,4-Benzoquinones. *J. Org. Chem.* **1982**, *47*, 2607−2613.
(28) Chavez, R., III; Cai, M.; Tlach, B.; Wheeler, D. L.; Kaudal, R.; Tsyrenova, A.; Tomlinson, A. L.; Shinar, R.; Shinar, J.; Jeffries-El, M. Benzobisoxazole Cruciforms: a Tunable, Cross-Conjugated Platform for the Generation of Deep Blue OLED Materials. *J. Mater. Chem. C* **2016**, *4*, 3765−3773.
(29) Aizpurua, J. M.; Palomo, C. Reagents and Synthetic Methods. 27: Improved Synthesis of 2-Substituted Benzoxazoles Induced by Trimethylsilyl Polyphosphate (PPSE). *Bull. Soc. Chim. Fr.* **1984**, 142−144.
(30) Yamamoto, K.; Watanabe, H. Composition of Polyphosphoric Acid Trimethylsilyl Ester (PPSE) and its Use as a Condensation Reagent. *Chem. Lett.* **1982**, *11*, 1225−1228.
(31) Hirata, S.; Totani, K.; Zhang, J.; Yamashita, T.; Kaji, H.; Marder, S. R.; Watanabe, T.; Adachi, C. Efficient Persistent Room Temperature Phosphorescence in Organic Amorphous Materials under Ambient Conditions. *Adv. Funct. Mater.* **2013**, *23*, 3386−3397.
(32) Cardona, C. M.; Li, W.; Kaifer, A. E.; Stockdale, D.; Bazan, G. C. Electrochemical Considerations for Determining Absolute Frontier Orbital Energy Levels of Conjugated Polymers for Solar Cell Applications. *Adv. Mater.* **2011**, *23*, 2367−2371.
(33) Salaneck, W. R. Classical Ultraviolet Photoelectron Spectroscopy of Polymers. *J. Electron Spectrosc. Relat. Phenom.* **2009**, *174*, 3−9.
(34) Miyamae, T.; Yoshimura, D.; Ishii, H.; Ouchi, Y.; Miyazaki, T.; Koike, T.; Yamamoto, T.; Muramatsu, Y.; Etori, H.; Maruyama, T.; Seki, K. Ultraviolet Photoelectron Spectroscopy of n-Type Conducting Polymers. *Synth. Met.* **1997**, *84*, 939−940.
(35) Lois, S.; Florès, J.-C.; Lère-Porte, J.-P.; Serein-Spirau, F.; Moreau, J. J. E.; Miqueu, K.; Sotiropoulos, J.-M.; Baylère, P.; Tillard, M.; Belin, C. How to Build Fully π-Conjugated Architectures with

DOI: 10.1021/acs.jpca.8b07778
J. Phys. Chem. A 2019, 123, 1343−1352

Thienylene and Phenylene Fragments. *Eur. J. Org. Chem.* **2007**, *2007*, 4019−4031.

DOI: 10.1021/acs.jpca.8b07778
J. Phys. Chem. A 2019, 123, 1343−1352